Fiber-Pigtailed Electrothermal MEMS Iris VOA

Hadi Veladi, Richard R. A. Syms, and Helin Zou

***Abstract*—A high-performance variable optical attenuator, which is based on an electrothermally actuated iris with a square pupil, is demonstrated. The device is fabricated from two separate dies that are formed by deep reactive ion etching of bonded silicon-on-insulator material. The iris die is inserted into an elastic clamp on a base-plate die carrying spring-mounted fiber alignment features, allowing the iris to be held in the optical path between two expanded core fibers. A novel aperture that dynamically reduces the clearances between the shutter blades is used to achieve an extinction of 25 dB and a wavelength dependent loss of ± 1 dB at 1550-nm wavelength. Synchronous blade motion is achieved using thermally optimized folded electrothermal actuators with undercut hot arms, which reduce the operating power to 240 mW and allow a high mechanical resonant frequency. Optical analysis is carried out using a scalar model and diffraction theory. Thermomechanical analysis is performed using a 1-D model and finite element simulation (ANSYS). Good agreement is obtained between the models and by experimentation.**

***Index Terms*—Microelectromechanical systems (MEMS), Micro-Opto-Electromechanical Systems (MOEMS), variable optical attenuator (VOA).**

I. Introduction

VARIABLE optical attenuators (VOAs) are required for level matching in wavelength division multiplexed optical communications [1], [2]. The main performance requirements are low insertion loss, high dynamic range, low wavelength and polarization dependence of loss (WDL and PDL), and low power consumption. Many different VOAs have been constructed using microelectromechanical system (MEMS) technology. Attenuation has been achieved by insertion of a shutter or a wedge and translation or tilt of a mirror; actuation has been achieved by electrostatic, electrothermal, and electromagnetic methods, and latching has been demonstrated [3]–[12]. Due to their symmetry, multiple-blade shutters offer the potential of extremely low WDL and PDL. By using expanded mode fibers [13], [14], alignment tolerances are considerably reduced; however, multiple actuators that are capable of stable operation over distances of up to ≈ 50 μm are then required. Two- and four-blade shutters have been demonstrated [15], [16]. In the latter case, synchronous motion of four electrothermal actuators was used to create a variable square pupil. However, due to the clearances between blades, the extinction was poor (17 dB). Furthermore, by using chevron-type buckling actuators [17], [18], the power consumption was very high (> 1.2 W), and the link beams used to suspend the shutters from the actuators introduced low-frequency resonances.

Dynamical motion of shaped features can drastically decrease clearances [19], while folded electrothermal actuators [20] can reduce drive powers and eliminate the need for link beams. An improved iris combining these features was recently presented [21]. Here, we demonstrate a high-performance fiber-pigtailed VOA based on this design, which combines an iris with a micromachined bench that holds an iris die and two expanded mode fibers in self-aligned mounts. In Section II, we introduce the mechanical, optical, and electrothermal design. In Section III, we describe fabrication, assembly, and measurement, and we demonstrate an extinction of 25 dB with a drive power of 240 mW. Conclusions are drawn in Section IV.

Manuscript received November 13, 2006; revised March 14, 2007.

H. Veladi was with the Optical and Semiconductor Devices Group, Electrical and Electronic Engineering Department, Imperial College London, SW7 2BT London, U.K. He is currently with the Electrical Engineering and Computer Department, Tabriz University, Tabriz 5166/15731, Iran.

R. R. A. Syms and H. Zou are with the Optical and Semiconductor Devices Group, Electrical and Electronic Engineering Department, Imperial College London, SW7 2BT London, U.K. (e-mail: r.syms@ic.ac.uk).

Digital Object Identifier 10.1109/JLT.2007.899788

II. Design

In this section, we introduce the main optical and mechanical features of the design. In the former case, we must consider the detailed layout of the iris and its effect on the coupling of a bounded beam between two fibers; in the latter case, optimization of the thermomechanical and dynamical behavior of the drive mechanism is considered.

A. Optical Design

The iris VOA uses synchronous motion of a set of shutters to create a variable polygonal aperture. Because of fabrication limitations—the minimum feature separation set by lithography and etching—there must be a finite clearance (typically, a few micrometers) between the blades. These clearances form slits, which allow transmission even in the "OFF" state. Smaller clearances can be realized using a method due to Fujita [19]. Adjacent parts are fabricated with a constant separation (usually the minimum achievable) but with dogleg perimeter patterns. When the parts are translated with respect to one another, relative motion of the doglegs can allow a smaller clearance over part of the working range.

By using this approach, we have developed the four-blade iris design shown in Fig. 1(a). The blades are broadly triangular but contain a dogleg feature on one edge. Each blade abuts two neighbors; therefore, there is a dogleg or zigzag between every pair. In contrast to the earlier design [16], which was "normally closed," this iris must be fabricated "normally open," as shown in position i). Assuming an original clearance $2s$ between the blades, the lateral offset $2s'$ of each dogleg is slightly smaller so that $2s' = 2(s - d)$. To actuate the iris, the blades are translated synchronously at 45° to the abutting edges

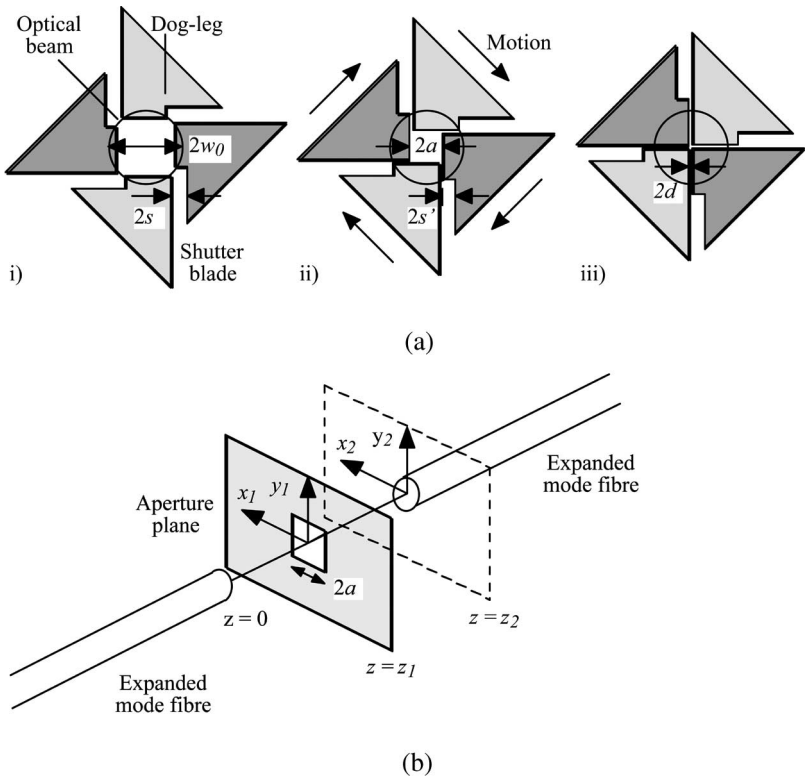

Fig. 1. Principle of iris VOA. (a) Operation of shaped-blade iris and (b) overall optical system.

to create a square pupil of width $2a$, acting on an optical beam (normally a Gaussian) of width $2w_0$. After a short distance, dogleg motion decreases the effective clearance to $2s'' = 2s - 2s' = 2d$, as shown in positions ii) and iii). The value of d can be determined at mask making and is not subject to the limits imposed by (for example) deep etching. Extinction is then limited by transmission through the four slits that remain when the iris is closed, as in position iii).

The optical performance of an iris VOA may be analyzed using a scalar theory. Fig. 1(b) shows the geometry, which consists of two optical fibers that are spaced apart along the z-axis with the iris between. The end of the input fiber lies at the origin, while the aperture and the output fiber are z_1 and z_2 away, respectively. Assuming that the fibers support a single Gaussian mode, the transverse electric field is $E_f = E_0 \exp(-r^2/w_0^2)$, where r is the radial distance. Ignoring diffraction, the effect of a perfect aperture may be described by limiting the field at its extremity. For a square pupil, the transmission is $T(x_1, y_1) = 1$ for $|x_1| \leq a$ and $|y_1| \leq a$, and $T(x_1, y_1) = 0$ for $|x_1| > a$ and $|y_1 > a$. The transverse field emerging from the pupil is then $E_a(x_1, y_1) = T(x_1, y_1)\, E_f(x_1, y_1)$. This beam is coupled into the output fiber with efficiency η, which is found as an overlap integral [22] as

$$\eta = |\langle E_a, E_f \rangle|^2 / \{\langle E_f, E_f \rangle\}^2 \tag{1}$$

where $\langle E_1, E_2 \rangle = \int \int_{\mathrm{A}} E_1 E_2^* dxdy$. In this case, we obtain [16]

$$\eta = \mathrm{erf}^4(\sqrt{2}a/w_0). \tag{2}$$

Equation (2) predicts zero transmission when $a/w_0 \to 0$ and a transmission tending to unity when a/w_0 rises above $\approx$2. In practice, finite blade clearances modify the transmission function, while diffraction modifies the amplitude and phase of the beam as it propagates. To investigate the effect of clearances, we may repeat the calculation leading to (2), assuming now that there are slots of final width $2d$ between the blades. In the closed state [position iii) in Fig. 1(a)], we obtain a minimum transmission of

$$\eta_{\min} = \mathrm{erf}^2(\sqrt{2}d/w_0)\left\{1 + \mathrm{erfc}(\sqrt{2}d/w_0)\right\}^2. \tag{3}$$

Fig. 2(a) shows the variation of the maximum attenuation $[-10\log_{10}(\eta_{\min})]$ with d/w_0. Clearly, the maximum attenuation is dramatically reduced as d/w_0 increases, and extinctions of > 20 dB can only be obtained for $d/w_0 < 0.04$. Small blade separations are therefore essential.

Diffraction degrades the performance still further, as we now show using the scalar theory [23]. Following the study in [24], the diffraction of an optical field E specified on the (x, y) plane to a field $E^\dagger$ on the $(x^\dagger, y^\dagger)$ plane a distance z away can be described by the integral

$$E^\dagger(x^\dagger, y^\dagger) = \iint_A \{f(\theta)/j\lambda R\}\, E(x, y) \exp(-jkR) dxdy. \tag{4}$$

Here, λ is the wavelength, $k = 2\pi/\lambda$, $R = \sqrt{\{(x^\dagger - x)^2 + (y^\dagger - y)^2 + z^2\}}$ is the distance between (x, y) and $(x^\dagger, y^\dagger)$,

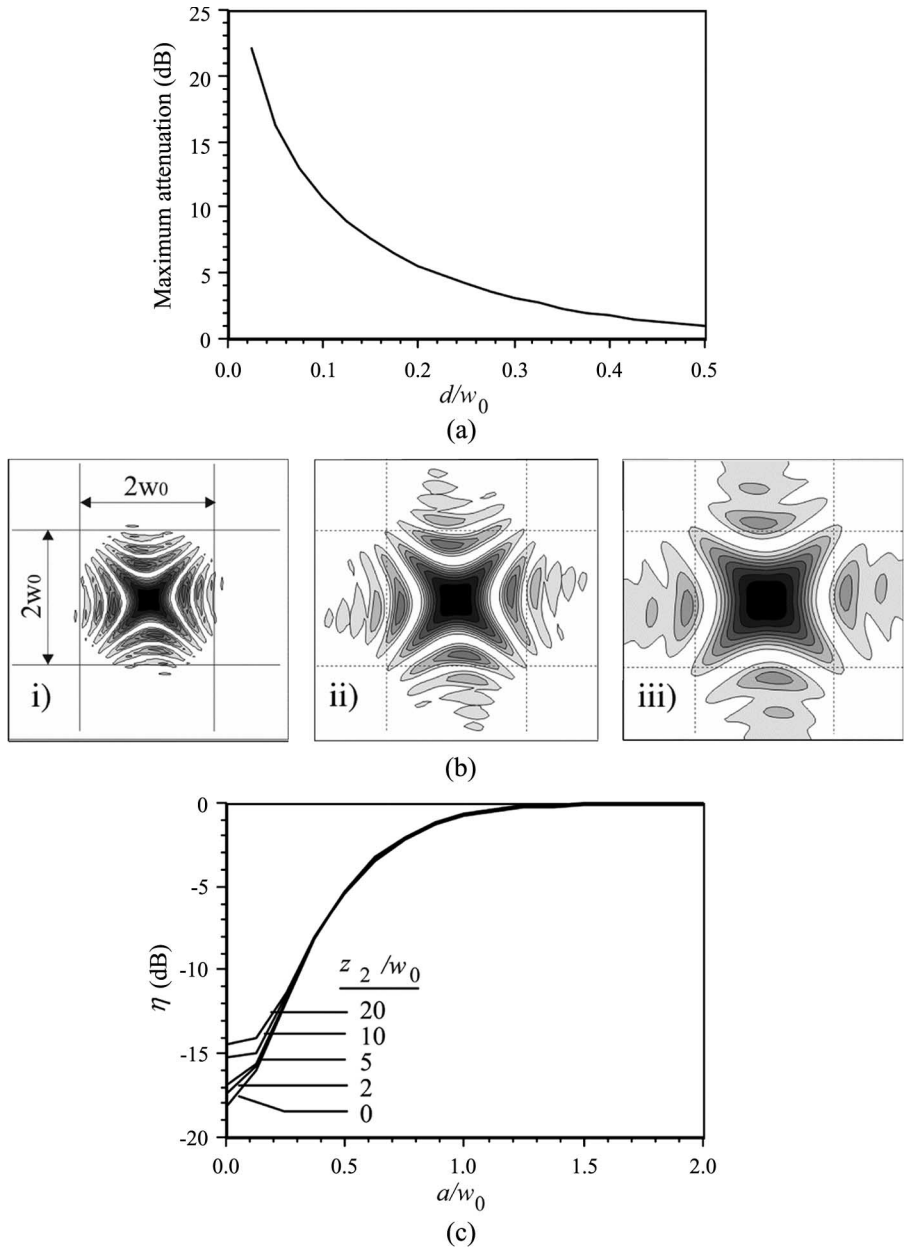

Fig. 2. (a) Variation of maximum attenuation with normalized slit size d/w_0, ignoring diffraction. (b) Diffraction patterns obtained in the closed state for different path lengths z_2. (c) Variation of transmission with normalized aperture size a/w_0 for different path lengths, as predicted by diffraction theory.

and $f(\theta)$ is a slowly varying function designed to exclude backward waves.

Equation (4) can be used to propagate the optical field from $z = 0$ to $z = z_1$, where it is modified by the transmission function and, then, to $z = z_2$, where the coupling efficiency can again be found as an overlap integral. Fig. 2(b) shows contours of constant intensity in the output fiber plane with the shutter in its closed state [position iii) in Fig. 1(a)] for different path lengths z_2. In each case, the mode field radius is $w_0 = 25$ μm, the wavelength is $\lambda = 1550$ nm, the initial normalized slit width is $s/w_0 = 0.12$, and the final normalized slit width is $d/w_0 = 0.04$. The iris is centrally placed so that $z_1 = z_2/2$, and the normalized path length is as follows: 1) $z_2/w_0 = 2$; 2) $z_2/w_0 = 5$; and 3) $z_2/w_0 = 10$. As the figures show, the power is concentrated near the axis when the optical path is small [Case i)] so that the overlap with the output mode is likely to be small. Power is spread over larger areas when the path increases [Cases ii) and iii)]. Since these distributions correspond more closely to the size and shape of the fiber mode, we might expect the extinction to be affected not only by the power transmitted by the aperture but also by the output beam shape. Fig. 2(c) shows the variation of transmission with aperture size a/w_0, as predicted by numerical evaluation of the diffraction integral, for the parameters in Fig. 2(b) and a wider range of path lengths. For zero path (no diffraction), a maximum attenuation of 18.5 dB is achieved when $a/w_0 = 0$. Transmission rises toward unity as a/w_0 increases so that $\eta > -1$ dB when a/w_0 is greater than about one. For longer paths, similar behavior can be seen. However, the maximum extinction is decreased to 17 dB when $z_2 = 5w_0$ and 14.5 dB when $z_2 = 20w_0$.

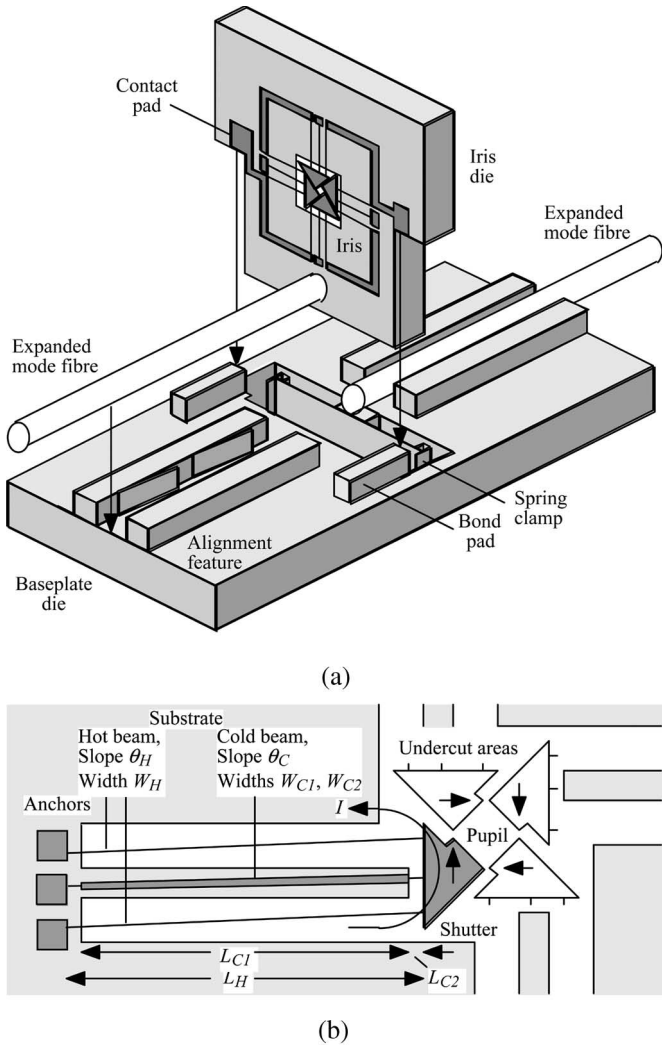

Fig. 3. (a) Construction of fiber-pigtailed iris VOA and (b) layout of single actuator of electrothermal shutter drive.

B. Package Design

The arguments above suggest that a mechanical arrangement with short path and small blade clearances (with respect to the mode size) is required for high extinction. The simplest solution—a very large mode—unfortunately requires collimating optics and long-travel actuators. Solutions must therefore be found for modest mode sizes, for example, those obtained directly from the expanded mode fiber [13], [14]. For $w_0 \approx 25$ μm, we require a separation between the fiber ends of $z_2 \approx 2w_0 \approx 50$ μm, and an actuator travel of $\sqrt{2} \times w_0 \approx 35$ μm. Such short paths can only be obtained easily using a micromachined package. Similarly, such long travel can only be achieved reliably with electrothermal actuators.

Fig. 3(a) shows the solution developed here. The iris is constructed on a silicon die carrying four electrothermal actuators that each supports one of the iris blades. The iris die is mounted in a silicon base, which is etched right though to provide a locating slot for the iris, self-alignment features, and a spring clamp. The slot is arranged at a small tilt to reduce return loss. The base plate also carries spring alignment features for two expanded mode fibers. These features allow axial motion so that the fibers may be brought up to the iris blades, locating the output fiber in a hole etched through the iris die. The iris actuators are connected as two parallel pairs of two series elements so that they may be driven synchronously from a common source. Electrical connection is made from the bond pads on the base plate to contacts on the iris die during assembly.

C. Electrothermal Design

The iris is operated using four folded electrothermal actuators, as shown in Fig. 3(b). Each actuator is composed of two parallel hot beams and one cold beam of length $L_{\rm H}$, which are fixed to anchors at one end and attached to a shutter blade at the other. The hot beams are of width $w_{\rm H}$ and inclined at an angle $\theta_{\rm H}$. The cold beam is of width $w_{\rm C1}$ for a length $L_{\rm C1}$ and $w_{\rm C2}$ for short sections $L_{\rm C2} = (L_{\rm H} - L_{\rm C1})/2$ at either end and is inclined at a larger angle $\theta_{\rm C}$. The device is actuated by passing a current I through the hot beams. To maximize the temperature rise, the substrate is etched away beneath the hot beams. The cold beam is heated only by solid conduction and cooled very effectively by gas conduction to the substrate. Consequently, its average temperature rise is considerably lower so that it impedes the expansion of the hot beams and forces a lateral displacement of the shutter. Since the actuator has only two hot beams, as compared with four in a chevron actuator, a twofold increase in electrothermal efficiency might be expected. However, by careful control of cooling, much larger improvements can be obtained, as we now show.

Initial design can be carried out using a 1-D model that includes electrical heating and the most important cooling modes. Radiation can be neglected, since peak temperatures are low. Here, we also ignore convection and concentrate on the effects of conduction cooling in the silicon and through the thin air layer trapped beneath the hot beam. In a 1-D model, the structure may be unfolded; therefore, the hot and cold beams are arranged sequentially along the x-axis, and parallel elements (the two hot beams) are combined. The iris blade itself may also be included as a short section.

Heating and cooling in the ith section may be modeled using the differential equation $k_{\rm Si}(w_i t_i)d^2T/dx^2 - k_{\rm Air}(w_i/g_i)T + I_i^2\rho_{\rm Si}/(w_i t_i) = 0$. Here, T is the temperature above ambient, x is the position along the beam, I_i is the heating current, w_i and t_i are the width and thickness of the ith section, and $k_{\rm Si}$ and $\rho_{\rm Si}$ are the thermal conductivity and resistivity of the material. The effect of any additional metal coatings was ignored, since these normally affect only the device resistance rather than the power sensitivity. Similarly, g_i is the thickness of the air beneath the ith section, and $k_{\rm Air}$ is its thermal conductivity. The term $I_i^2\rho_{\rm Si}/(w_i t_i)$ may also be written as P_i/L_i, where P_i and L_i are the heating power and length of the ith section. The boundary conditions are that $T = 0$ at the anchors and that the heat flow $k_{\rm Si}(w_i t_i)dT/dx$ is continuous between sections. The heat conduction equation may be solved analytically by coupling together solutions for each section. However, for N sections, $2N$ simultaneous equations must be solved to satisfy the boundary conditions. Since the process is laborious, we have used a numerical solution, integrating the equation directly. Throughout, we assume a power of

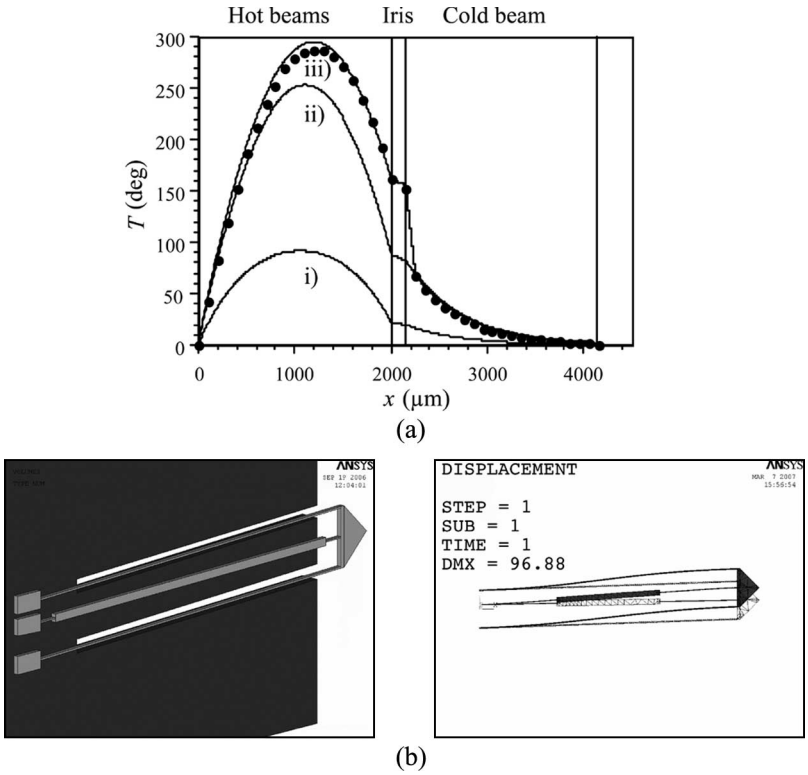

Fig. 4. (a) Theoretical temperature profile $T(x)$ along the hot and cold beams of electrothermal actuators with three different designs. i) and ii) Constant width cold beam, without and with substrate removal beneath the hot beams; iii) variable width cold beam, with substrate removal beneath the hot beams. Full lines: One-dimensional theory; crosses: Result of finite element modeling. (b) ANSYS model of static and resonant actuator.

50 mW, a thickness of $t = 25$ μm, and a thermal conductivity of $k_{\rm Si} = 150$ W $\cdot$ m^{-1} $\cdot$ °C^{-1} for silicon and a conductivity of $k_{\rm Air} = 0.03$ W $\cdot$ m^{-1} $\cdot$ °C^{-1} for air.

Fig. 4(a) shows the temperature variation along the beam for three different cases. In each case, we assume that the hot beams are narrow, while the cold beam is much wider so that it may be effectively cooled. In Case i), we assume a hot arm length and width of $L_{\rm H} = 2000$ μm and $w_{\rm H} = 8$ μm. We assume that the cold arm is of uniform width so that $L_{\rm C1} = L_{\rm H}$ and $w_{\rm C1} = 40$ μm. The shutter is a 45° triangle with hypotenuse of 150 μm. The hot and cold beams are both initially assumed to have the same thin air gap of $g_{\rm H} = g_{\rm C} = 2.5$ μm. The temperature variation is approximately parabolic in the hot beams and exponential in the cold beam. However, the average temperature difference ΔT between the two is small. In Case ii), we assume similar parameters, but the air gap beneath the hot beams and blade is increased to $g_{\rm H} = 500$ μm to model substrate removal. The hot beam temperature is now much higher due to the elimination of gas conduction. In Case iii), we assume also that the cold beam is of variable width, with a central section of length $L_{\rm C1} = 1800$ μm and width $w_{\rm C1} = 40$ μm, and short narrow sections of length $L_{\rm C2} = 100$ μm and width $w_{\rm C2} = 6$ μm at either end. The section near the hot beams is also undercut. These sections allow a further temperature rise in the hot beams and provide the flexibility needed for motion. The simple model above can be verified by finite element analysis. For example, Fig. 4(b) shows an actuator layout constructed using the commercial package ANSYS R6.0. Elements of type SOLID70 were used to perform thermal analysis. The boundary conditions were $T = 0$ at the anchors and at the substrate beneath the suspended beams. The parameters are as in Case iii), assuming also that $\theta_{\rm H} = 1°$ and $\theta_{\rm C} = 2°$. The discrete data superimposed on Fig. 4(a) represent the ANSYS prediction and are in excellent agreement with the simple model.

Inclusion of radiation and convection, although possible, complicates the analysis and requires knowledge of unknown heat transfer coefficients. In that event, reasonable agreement with later experimental results was obtained with the simple model assumed.

Optimization of this concept is possible. For example, Fig. 5(a) shows the variation of the average temperature difference ΔT with the ratio $\beta = 2L_{\rm C2}/L_{\rm H}$ for a fixed power of 50 mW. ΔT rises gradually, peaking when $\beta = 0.6$. Ignoring structural considerations, the greatest electrothermal efficiency is likely to be obtained at this point. However, efficiency may not be the only criterion. For example, improving the efficiency by minimizing the amount of cooling will inevitably increase response times. In addition, the travel range of a thermal actuator is usually limited by damage, and it is therefore important to maximize the value of $\Delta T/T_{\rm max}$, where $T_{\rm max}$ is the highest temperature attained. Fig. 5(a) also shows the variation of $\Delta T/T_{\rm max}$ with β, which peaks at $\beta = 0.15$. Designs in the rough range $0.1 < \beta < 0.6$ are therefore likely to be suitable.

D. Mechanical Design

In principle, the Euler bending equation $d^2y_i/dx^2 = \Sigma M_i/EI_i$ may be used to model the elastic response of the actuator, taking into account thermal expansion and axial loads, and assuming appropriate boundary and displacement compatibility

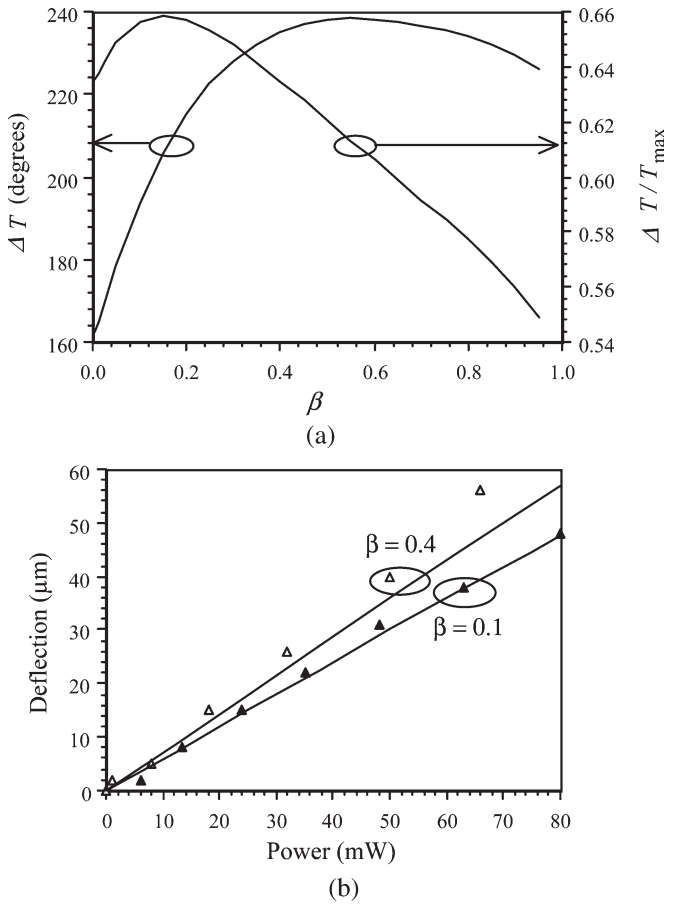

Fig. 5. (a) Theoretical variation of the average temperature difference ΔT and its normalized equivalent $\Delta T/T_{\max}$ with the length ratio of $\beta = 2L_{C2}/L_{H}$. (b) Theoretical (solid lines) and experimental (discrete points) variation of displacement with electrical drive power for two individual actuators, with $\beta = 0.1$ and 0.4, respectively.

conditions. Here, y_i is the deflection of the ith element at x, ΣM_i is the sum of the moments acting, E is Young's modulus, and $I_i = t_i w_i^3/12$ is the second moment. This approach has already been used to model the chevron actuator [18]. However, because the cold beam here is a multisection element, while the link beam both rotates and carries axial and transverse loads, a full solution involves a significant number of simultaneous equations, some of which are nonlinear.

We have therefore used ANSYS to find the deflection, assuming a Young's modulus of $E = 1.65 \times 10^{11}$ N $\cdot$ m^{-2}, a Poisson's ratio of $\nu = 0.22$, and a thermal expansion coefficient of $\alpha = 1.06 \times 10^{-6}$ °C^{-1} for silicon. Elements of type SOLID 45 were used for the structural analysis, and all displacements at the anchors were zero. The full lines in Fig. 5(b) show the variation of deflection with power for Case iii) ($\beta = 0.1$), as well as for a variant with $\beta = 0.4$. Here, the thickness has been reduced to 21 μm for comparison with the experimental results in the next section. The characteristics are linear in contrast to chevron actuators [17], [18], and (for example) 40-μm deflection is predicted for 60-mW power. This result suggests an operating power of 240 mW for a complete iris with four similar actuators.

ANSYS may also be used to find the resonant modes. Fig. 4(b) also shows the shape of the lowest order mode for Case iii) ($\beta = 0.1$). The resonant frequency is 6780 Hz. The corresponding frequency for a device with $\beta = 0.4$ is slightly lower (6020 Hz), which is due to the reduced stiffness of the cold beam. However, in each case, the high resonant frequency suggests a low sensitivity to environmental disturbances.

III. Fabrication and Testing

In this section, we describe the design, fabrication, and assembly of experimental iris VOAs and present the results of electromechanical and optical characterization.

A. Design Parameters

Devices were constructed using actuators with the dimensions of the previous section, including variants with $\beta = 0.1$ and $\beta = 0.4$. The initial iris width $2a$ was 56 μm so that an actuator travel of $56/\sqrt{2} \approx 40$ μm was required to close the iris completely. The blade clearances were $2s = 6$ μm at fabrication, reducing to $2d = 2$ μm during operation, after an actuator travel of $\approx$6 μm. The iris die size was 7.4×6.2 mm^2, while the base-plate die measured 14.6×6.6 mm^2.

B. Fabrication

Devices were fabricated by deep reactive ion etching of 100-mm-diameter 450-μm-thick (100) orientated bonded silicon-on-insulator (BSOI) wafers [25]. Different wafers were used for the iris and base-plate dies. Nominal bonded layer thicknesses of 25 and 85 μm were used for the former and latter, respectively; however, inspection after processing revealed that the former value was only $t = 21$ μm. The interlayer oxide thickness was $g = 2.5$ μm. Fabrication was based on double-sided lithography, followed by etching in a Surface Technology Systems single-chamber multiplex inductively coupled plasma etcher. After the removal of the sacrificial oxide layer by wet etching in buffered HF, the wafers were freeze dried in a vacuum chamber to sublime water vapor from the solid phase and allow residual rinse water to be safely removed from beneath the suspended parts. This process prevents the parts from being pulled down to the nearby substrate by surface tension forces. The electrical conductivity of the suspended parts was then increased using a sputtered layer of 300-Å Cr and 1000-Å Au metal. Isolation between parts was ensured by the long undercut etch, which prevented metal tracking over the supporting oxide. All the suspended parts therefore consist of metal-coated silicon, supported above the substrate on small pads of residual oxide. Fig. 6(a) and (b) shows a complete iris die; the blade alignment is clearly well preserved after the release step.

C. Assembly

To carry out the assembly, the substrate was first mounted on a PCB (which contained an etched slot to allow clearance for the iris die), and wirebond connections were made to the bond pads. The iris die was then inserted into its mounting slot using two manipulators to retract the spring clamp and a third for positioning. Once the iris was in place, the spring

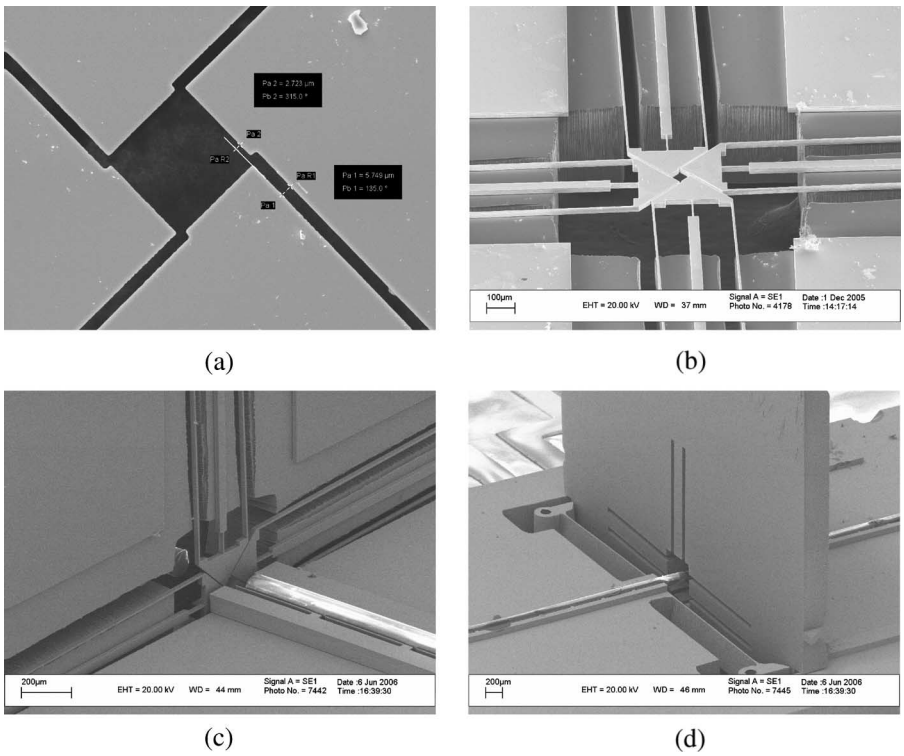

Fig. 6. SEM photographs of (a) and (b) iris element and (c) and (d) front and rear of pigtailed VOA.

clamp was released, and the electrical connections were made to the base plate using conductive epoxy. Expanded mode fibers (TEC fibers, with a mode size of $w_0 = 25$ μm, from Kadence Photonics) were then mounted in the fiber alignment grooves. With the blade clearances used, $d/w_0 = 1/25 = 0.04$. Fig. 6(c) shows a completed iris VOA. The input fiber is on the right-hand side, while the iris is at the center of the photograph; the output fiber can be seen just behind the iris. Fig. 6(d) shows the elastic clamp behind the iris die.

D. Characterization

The mechanical performance of a single actuator was first evaluated using an optical microscope with a video camera and a cursor measurement system. Fig. 5(b) also shows the static variation of blade displacement with drive power, which is superimposed on the ANSYS model prediction. For the device with $\beta = 0.1$, the agreement is extremely good after correction of the mechanical thickness; however, higher than expected deflections are obtained for $\beta = 0.4$. Fig. 7(a) shows the variation of peak-to-peak deflection with electrical drive frequency under sinusoidal excitation for both devices. Since the device is power-driven, the mechanical response is at twice the frequency shown. A rolloff associated with the first-order response of the electrothermal drive can be seen at 40 Hz for the device with $\beta = 0.1$; this value is reduced to 20 Hz for $\beta = 0.4$, suggesting the usual compromise between speed and efficiency inherent in thermal excitation. Similarly, a deflection peak associated with the second-order response of the shutter and its suspension can be seen at 3.4 kHz (corresponding to a mechanical resonance of 6.8 kHz, in agreement with the earlier ANSYS prediction) for $\beta = 0.1$. This value is again lowered for the device with $\beta = 0.4$, due to its reduced mechanical stiffness, but is more than predicted by ANSYS. One explanation is lateral etching, which will have a greater effect on long narrow beams.

The dynamic performance was verified using pigtailed VOAs, using an Agilent 83438A broadband erbium ASE source operating near $\lambda = 1550$ nm. A square-wave input was applied to the shutter drive, and the instantaneous optical output power was detected using a Ge photodetector. Fig. 7(b) shows the result for a square-wave input of 7-V peak and 40-Hz frequency for a device with $\beta = 0.1$. The iris is normally open. As each voltage step is applied, the transmission decreases exponentially, with a time constant of about 6 ms. The latency is the same for the falling edge of signal and limits the upper modulation frequency to $1/(12 \times 10^{-3}) = 80$ Hz, which is in agreement with the figure of 40 Hz above. There is no sign of oscillations due to mechanical resonance.

The optical performance of pigtailed VOAs was then assessed using an Agilent 86140B optical spectrum analyzer and an Agilent 83437A broadband LED source. The insertion loss was first measured at a fixed wavelength ($\lambda = 1550$ nm) as 0.75 dB. The static transfer characteristics were then measured at the same wavelength; Fig. 8(a) shows the results for a device with $\beta = 0.1$. The drive power is larger than that shown in Fig. 5(b), because all four actuators are now operating together. The attenuation increases as the iris closes, and a maximum attenuation is obtained at 240-mW drive power, which is in agreement with the ANSYS prediction and representing an approximate fivefold reduction in drive power over the earlier design [16]. The transmission can increase again after this point, because the shutters can continue to slide past each other; however, this possibility could easily be eliminated using a mechanical "stop." The maximum attenuation is $\approx$25 dB, which is

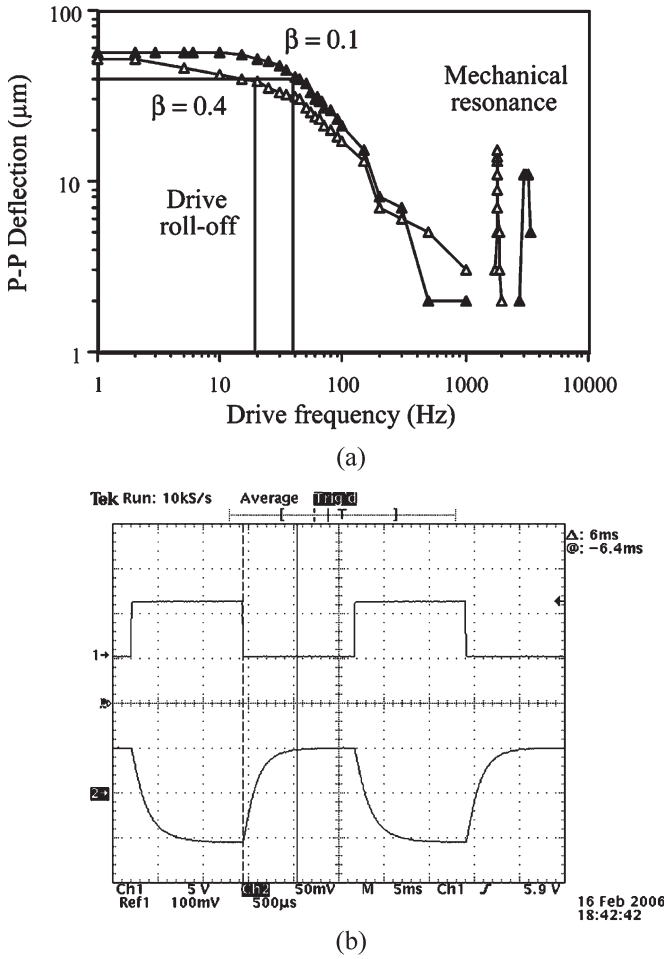

Fig. 7. (a) Frequency responses and (b) step response of completed iris VOAs.

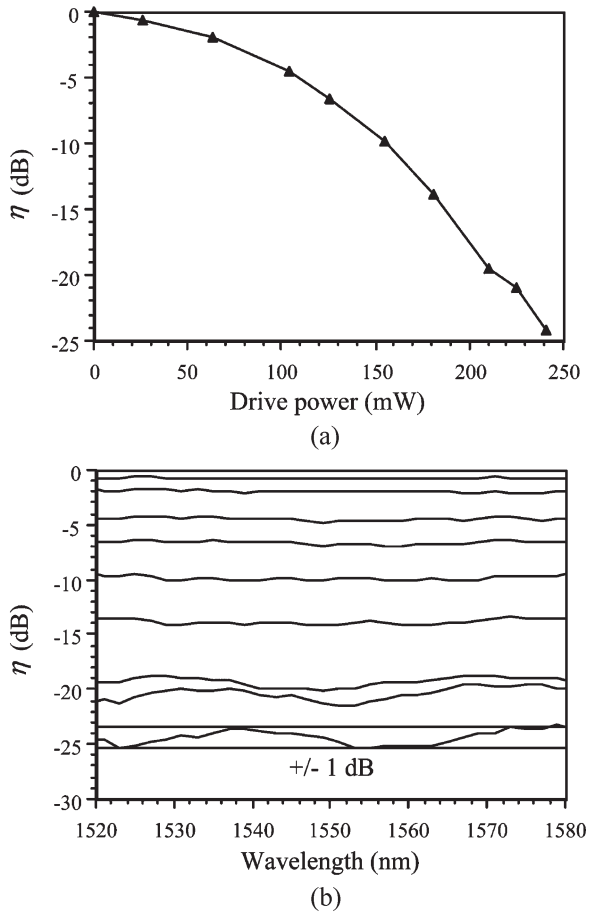

Fig. 8. Variation of optical transmission with (a) power and (b) wavelength for completed iris VOAs.

slightly more than expected from the theoretical analysis, and ≈8 dB greater than achieved with the earlier design [16].

The wavelength dependence of performance was then measured. Fig. 8(b) shows the spectral variation of transmission at different attenuation levels. The variation is generally flat, but as the attenuation rises, an increasing quasi-periodic variation may be seen. At 25-dB attenuation, the amplitude and period are ≈1 dB and $\Delta\lambda \approx 40$ nm. This behavior is a characteristic of an air-spaced cavity between weakly reflecting surfaces. The cavity spacing $d = \lambda^2/2\Delta\lambda \approx 30\ \mu$m is approximately the spacing of the TEC fibers from the VOA blades, suggesting poor control of internal reflections.

IV. Conclusion

A new four-blade iris-type VOA has been demonstrated using MEMS technology. Improved optical characteristics have been obtained using shutter blades that are shaped to reduce clearances dynamically. Reduced drive power is obtained by using folded electrothermal actuators and by using substrate removal and layout optimization to restrict conduction cooling. Fiber pigtailing is carried out using a micromachined base plate that mounts the iris and two expanded mode fibers in self-aligned sprung alignment features. Prototypes have been fabricated by deep reactive ion etching of BSOI. Experimental measurements at 1550-nm wavelength show a maximum attenuation of 25 dB, a drive power of 240 mW, and a bandwidth of 40 Hz. These results are in good agreement with the theoretical analysis carried out using analytical and numerical modeling. Wavelength dependent loss is currently limited to around ±1 dB at high attenuation by reflections.

There is some scope for performance improvement. Since the power consumption of an electrothermal drive scales with its thickness, drive powers could be reduced further, simply by reducing the bonded layer thickness. Further reductions in power could also be achieved by minimizing unwanted cooling, albeit at the cost of an increase in response time. This tradeoff can clearly be avoided using an alternative electrostatic drive, although the increased mass associated with the drive electrode is likely to lower the natural resonant frequency considerably and introduce the possibility of large undamped transients. Optical extinction could be improved by reducing the structural thickness, since this would allow a further reduction in the separation between the shutter blades. Finally, the wavelength dependent loss could be reduced using an increased iris tilt.

References

[1] K. C. Nguyen, "MEMS components for WDM transmission systems," in *Proc. OFC*, Mar. 17–22, 2002, pp. 89–90.

[2] C. Gu, Y. Xu, P. J. J. Liu, F. Zhou, L. Dong, and H. He, "Fiber based devices for DWDM optical communication systems," *Proc. SPIE*, vol. 5642, pp. 6–18, 2005.

[3] B. Barber, C. R. Giles, V. Askyuk, R. Ruel, L. Stulz, and D. Bishop, "A fiber connectorized MEMS variable optical attenuator," *IEEE Photon. Technol. Lett.*, vol. 10, no. 9, pp. 1262–1264, Sep. 1998.
[4] C. Marxer, P. Griss, and N. F. Rooij, "A variable optical attenuator based on silicon micromechanics," *IEEE Photon. Technol. Lett.*, vol. 11, no. 2, pp. 233–235, Feb. 1999.
[5] R. Wood, V. R. Dhuler, and E. A. Hill, "MEMS variable attenuator," in *Proc. IEEE/LEOS Int. Conf. Opt. MEMS*, Kauai, HI, Aug. 21–24, 2000, pp. 121–122.
[6] C.-H. Kim, N. Park, and Y. K. Kim, "MEMS reflective type variable optical attenuator using off-axis misalignment," in *Proc. IEEE LEOS Int. Conf. Opt. MEMS*, Lugano, Switzerland, Aug. 20–23, 2002, pp. 55–56.
[7] C. Marxer, B. D. Jong, and N. D. Rooij, "Comparison of MEMS variable optical attenuator designs," in *Proc. IEEE/LEOS Int. Conf. Opt. MEMS*, Lugano, Switzerland, Aug. 20–23, 2002, pp. 189–190.
[8] C.-H. Ji, Y. Yee, J. Choi, and J.-U. Bu, "Electromagnetic variable optical attenuator," in *Proc. IEEE/LEOS Int. Conf. Opt. MEMS*, Lugano, Switzerland, 2002, pp. 49–50.
[9] S. Sumriddetchkajorn and N. A. Riza, "Fault-tolerant three-port fiber-optic attenuator using small tilt micromirror device," *Opt. Commun.*, vol. 205, no. 1–3, pp. 77–86, Apr. 2002.
[10] J. H. Lee, Y. Y. Kim, S. S. Yun, H. Kwon, Y. S. Hong, J. H. Lee, and S. C. Jung, "Design and characteristics of a micromachined variable optical attenuator with a silicon optical wedge," *Opt. Commun.*, vol. 221, no. 4–6, pp. 323–330, Jun. 2003.
[11] X. M. Zhang, A. Q. Liu, C. Lu, F. Wang, and Z. S. Liu, "Polysilicon micromachined fiber-optical attenuator for DWDM applications," *Sens. Actuators A, Phys.*, vol. 108, no. 1–3, pp. 28–35, Nov. 2003.
[12] R. R. A. Syms, H. Zou, J. Stagg, and D. F. Moore, "Multi-state latching MEMS variable optical attenuator," *IEEE Photon. Technol. Lett.*, vol. 16, no. 1, pp. 191–193, Jan. 2004.
[13] H. Hanafusa, M. Horiguchi, and J. Noda, "Thermally-diffused expanded core fibers for low-loss and inexpensive photonic components," *Electron. Lett.*, vol. 27, no. 21, pp. 1968–1969, Oct. 1991.
[14] M. Kihara, M. Matsumoto, T. Haibara, and S. Tomita, "Characteristics of thermally expanded core fiber," *J. Lightw. Technol.*, vol. 14, no. 10, pp. 2209–2214, Oct. 1996.
[15] L. Li and D. Uttamchandani, "Design and evaluation of a MEMS optical chopper for fibre optic applications," *Proc. Inst. Electr. Eng.—Sci. Meas. Technol.*, vol. 151, no. 2, pp. 77–84, Mar. 2004.
[16] R. R. A. Syms, H. Zou, J. Stagg, and H. Veladi, "Sliding-blade MEMS iris and variable optical attenuator," *J. Micromech. Microeng.*, vol. 14, no. 12, pp. 1700–1710, Dec. 2004.
[17] M. J. Sinclair, "A high force low area MEMS thermal actuator," in *Proc. 7th ITHERM*, Las Vegas, NV, May 23–26, 2000, pp. 127–132.
[18] L. Que, J. Park, and Y. B. Gianchandani, "Bent-beam electrothermal actuators—Part I: Single beam and cascaded devices," *J. Microelectromech. Syst.*, vol. 10, no. 2, pp. 247–254, Jun. 2001.
[19] T. Hirano, T. Furuhata, K. J. Gabriel, and H. Fujita, "Design, fabrication, and operation of submicron gap comb-drive microactuators," *J. Microelectromech. Syst.*, vol. 1, no. 1, pp. 52–59, Mar. 1992.
[20] R. R. A. Syms, H. Zou, J. Yao, D. Uttamchandani, and J. Stagg, "Scalable electrothermal MEMS actuator for optical fibre alignment," *J. Micromech. Microeng.*, vol. 14, no. 12, pp. 1633–1639, Dec. 2004.
[21] H. Veladi, R. R. A. Syms, and H. Zou, "Low power, high extinction electrothermal MEMS iris VOA," *Proc. SPIE*, vol. 6186, pp. 61 860J.1–61 860J.12, 2006. paper 18.
[22] R. R. A. Syms and J. R. Cozens, *Optical Guided Waves and Devices*. London, U.K.: McGraw-Hill, 1992.
[23] X. H. Dai, X. L. Zhao, B. C. Cai, and Y. Cao, "Modelling and characterization of diffractive optical propagation inside MEMS variable optical attenuator," *Proc. SPIE*, vol. 4920, pp. 148–151, 2002.
[24] M. Born and E. Wolf, *Principles of Optics*, 6th ed. Oxford, U.K.: Pergamon, 1980.
[25] E. H. Klaassen, K. Petersen, J. M. Noworolski, J. Logan, N. I. Maluf, J. Brown, C. Storment, W. McCulley, and T. A. Kovacs, "Silicon fusion bonding and deep reactive ion etching: A new technology for microstructures," *Sens. Actuators A, Phys.*, vol. 52, no. 1–3, pp. 132–139, Mar. 1996.

Hadi Veladi was born in Tabriz, Iran, in 1968. He received the B.Sc. degree in electrical engineering from Tabriz University, the M.Sc. degree in computer engineering from Amirkabir University of Technology, Tehran, Iran, and the Ph.D. degree in microsystems technology from the Imperial College London, London, U.K., in 2006.

He is currently an Assistant Professor with the Electrical and Computer Engineering Department, Tabriz University. His main areas of interest include MEMS technology for microoptical devices and high-performance electrothermal actuators and their application in adaptive optic, optical filters, and polymer devices.

Richard R. A. Syms was born in Norfolk, VA, in 1958. He received the B.A. degree in engineering science and the D.Phil. degree (on volume holographic optical elements) from Worcester College, Oxford, U.K., in 1979 and 1982, respectively.

He has been the Head of the Optical and Semiconductor Devices Group in the EEE Department, Imperial College London, London, U.K., since 1992, and a Professor of microsystems technology since 1996. He has published over 100 journal papers and two books on holography, integrated optics, laser and amplifier devices, and microengineering. He is a Cofounder and Research Director of the MEMS spin-out company Microsaic Systems.

Prof. Syms currently acts as an Associate Editor for the *IEEE/ASME Journal of Microelectromechanical Systems*. He is a Fellow of the IEE, the Institute of Physics, and the Royal Academy of Engineering.

Helin Zou was born in Liaoning, China, in 1954. He received the B.S. degree in applied physics and the M.Eng. degree in semiconductor physics from Dalian University of Technology, Dalian, China, in 1982 and 1987, respectively, and the Ph.D. degree in thermoelectronics engineering from the University of Wales, Cardiff, U.K., in 2001.

Since June 2001, he has been a Postdoctoral Research Associate with the Department of Electrical and Electronic Engineering, Imperial College London, London, U.K. His research interests focus on the microfabrication technology for MEMS. He has contributed over 30 research publications in the MEMS and semiconductor thin films and devices area.